Original Article
cnj.araku.ac.ir

☑ Cite This: Colloid Nanosci. J. 3(2) (2025) 602-609 DOI: 10.61882/CNJ.3.2.602

Defect Engineering and 2D/2D Coupling in Mn- and B-Doped BiVO4 and Ti_3C_2 Nanostructures

Mahjoobeh Bidueinezhad, Fariba Fathirad*

Department of Nanotechnology, Graduate University of Advanced Technology, Kerman, Iran

ARTICLE INFO

Article History:
Received 2025-08-19
Revised 2025-09-29
Accepted 2025-11-06

Corresponding Authors:
Fariba Fathirad
Email:
f_fathirad@yahoo.com

ABSTRACT

Doping is an effective method that modulates the electronic and optical properties of semiconductor nanomaterials through the addition of foreign atoms. In this work, bismuth vanadate ($BiVO_4$) and titanium carbide (Ti_3C_2) MXene nanosheets were synthesized through facile solution processes. To elucidate the roles of defect engineering and 2D/2D interfacial coupling, a series of systems including Mn-BiVO4, B-Ti_3C_2, Ti_3C_2/$BiVO_4$, Mn-$BiVO_4$/Ti_3C_2, $BiVO_4$/B-Ti_3C_2, and Mn-$BiVO_4$/B-Ti_3C_2 were synthesized and characterized by XRD, FTIR, FESEM, and EDX. DRS results reveal that Mn and B doping, as well as the construction of the heterostructure, lower the optical band gap from 2.9 eV (pristine $BiVO_4$/Ti_3C_2) to 2.4 eV (Mn-$BiVO_4$/B-Ti_3C_2). . These controlled defect states and 2D/2D interfaces enhance charge separation and photoactivity, demonstrating the potential of Mn-$BiVO_4$/B-Ti_3C_2 for photo-driven redox applications.

KEYWORDS: *Ti_3C_2 MXene, Doping, Heterostructures, Photoactivity*

1. Introduction

MXenes represent a novel class of two-dimensional (2D) nanomaterials, composed of transition metal carbides, nitrides, or carbonitrides, with the general formula $M_{n+1}X_n$, where M denotes an early transition metal and X correspond to carbon and/or nitrogen [1,2]. Since their initial discovery in 2011, the diversity of MXenes has significantly expanded, leading to extensive investigations into their physicochemical properties and potential applications. [3,4]. Titanium carbide (Ti_3C_2) is one of the most popular among them due to its ability to attract water, electrical conductivity, high surface area, stability in chemicals, and biocompatibility. It also possesses a tunable electronic band structure. These characteristics render Ti_3C_2 MXene suitable for applications in energy storage, catalysis, and electronics [5,6]. Ti_3C_2 is typically prepared through the selective etching of Ti_3AlC_2 MAX phase precursors. This process results in 2D nanosheets bearing numerous surface groups (–OH, –O, –F) that facilitate their ability to disperse in water and strengthen their interaction with other nanomaterials [7-9].

Bismuth vanadate ($BiVO_4$) is an n-type semiconductor with a band gap of ~2.4 eV, which is stable, inexpensive, and environmentally friendly, making it a promising material for photoelectrochemical (PEC) water splitting [10–12]. Pristine $BiVO_4$, however, is plagued by inefficient charge transport and fast electron–hole recombination, resulting in low photocatalytic efficiency [13–15]. To overcome these limitations, various strategies have been suggested, including foreign element doping and coupling with highly conductive 2D nanostructures. Doping can tailor the electronic structure through the introduction of defect states, which can improve carrier diffusion, conductivity, and light harvesting [16-22]. Substitutional metal dopants, in particular,

have been found to enhance photoactivity through the elongation of carrier lifetimes and adjustment of band positions [23-25]. Hybridization with conductive nanosheets like Ti_3C_2 MXene, on the other hand, promotes interfacial charge separation and directional electron transport, providing another avenue for performance improvement [26-30]. In this research, we synthesized a series of nanostructures comprising pure Ti_3C_2 and $BiVO_4$, Mn-doped $BiVO_4$ (Mn-$BiVO_4$), B-doped Ti_3C_2 (B-Ti_3C_2), and their hybrids (Ti_3C_2/$BiVO_4$, Mn-$BiVO_4$/Ti_3C_2, $BiVO_4$/B-Ti_3C_2, and Mn-$BiVO_4$/B-Ti_3C_2) via solution-based processes. We conducted examinations on their structure, morphology, and optical properties. Therefore, our work reports a dual-defect/dual-2D coupling design strategy that systematically demonstrates how Mn and B dopants, coupled with Ti_3C_2-$BiVO_4$ nanosheet coupling, cooperatively modulate the structure property relationship.

2. Experimental

2.1. Materials and apparatus

The Ti_3AlC_2 MAX phase precursor was procured from Redox Kala Co. (Iran). All other chemicals used in this study were of analytical grade and obtained from Merck, including hydrofluoric acid (HF, 40%), sodium metavanadate ($NaVO_3$, ≥99%), bismuth(III) salt ($Bi_5H_9N_4O_{22}$), cetyltrimethylammonium bromide (CTAB, ≥99%), boric acid (H_3BO_3, ≥99.5%), manganese(II) nitrate tetrahydrate ($Mn(NO_3)_2{\bullet}4H_2O$, ≥98%), ethylene glycol ($C_2H_6O_2$, ≥99%), ethanol (C_2H_5OH, 96%), sulfuric acid (H_2SO_4, 98%), and ammonium metavanadate (NH_4VO_3, ≥99%). Deionized water (DIW) was used throughout the synthesis processes to ensure the purity of the nanostructures. The synthesized nanomaterials were characterized using various advanced analytical techniques. Fourier-transform infrared (FTIR) spectra were recorded on a Bruker Tensor 27 spectrometer to identify the functional groups and confirm the chemical composition. The crystallographic structure and phase purity of the synthesized samples were analyzed using an X-ray diffractometer (Rigaku D-max C III, Cu Kα radiation, λ = 1.5406 Å). The surface morphology and elemental composition were examined via field-emission scanning electron microscopy (FESEM) and energy-dispersive X-ray spectroscopy (EDX) using a MIRA3 TESCAN-XMU instrument. The optical properties and electronic band structure modifications were investigated through diffuse reflectance spectroscopy (DRS) using a Shimadzu UV-160A spectrophotometer.

2.2. Synthesis of Ti_3C_2 and B-Ti_3C_2

Ti_3C_2 MXene nanosheets were synthesized through a modified selective etching process. 1 g of Ti_3AlC_2 MAX phase powder was added slowly into 10 mL of 40% hydrofluoric acid (HF) under continuous stirring at 25 °C for 24 h. The resulting dark suspension was centrifuged, and the precipitate was washed several times with deionized water (DIW) until the supernatant pH was close to 6.0. The thus purified Ti_3C_2 was dried in a vacuum oven at 60 °C for 12 h. For exfoliation, the powder of Ti_3C_2 was dispersed in 40 mL of the binary solvent system dimethyl sulfoxide (DMSO) and ethanol (1:1 v/v). The dispersion was stirred at room temperature for 1.5 h, followed by probe sonication (400 W, 7 s on/3 s off) for 30 min to achieve delamination of the layered structure of Ti_3C_2. The resulting suspension was centrifuged at 5000 rpm for 10 min, washed repeatedly with DIW to remove the residual solvents, and finally centrifuged at low speed (1000 rpm, 10 min) to collect the supernatant containing the exfoliated Ti_3C_2 nanosheets with colloidal stability in solution.

Boron-doped Ti_3C_2 (B–Ti_3C_2) nanostructures were synthesized via a hydrothermal doping process. Typically, 0.1 g of Ti_3C_2 MXene was suspended in 25 mL of 0.1 M aqueous boric acid (H_3BO_3) solution and ultrasonicated (40 kHz, 20 min) for uniform dispersion. The suspension was poured into a Teflon-lined stainless-steel autoclave and maintained at 200 °C for 5 h under autogenous pressure. After the cooling to room temperature naturally, the B–Ti_3C_2 MXene was collected, washed with DIW, and dried under vacuum at 80 °C. The concentration of boric acid precursor was carefully controlled to maintain consistent doping levels. The synthesis was repeated, yielding samples with reproducible XRD and FTIR features.

2.3. Synthesis of $BiVO_4$ and Mn-$BiVO_4$

$BiVO_4$ nanosheets were synthesized by a hydrothermal route, as reported in our previous work [31]. Manganese-doped $BiVO_4$ (Mn–$BiVO_4$) was prepared by doping Mn^{2+} into the $BiVO_4$ lattice through a controlled doping procedure. In a standard synthesis, 0.02 g of $Mn(NO_3)_2{\cdot}4H_2O$ (equivalent to ~2 mol% relative to Bi^{3+}) was dissolved in 10 mL of deionized water and dripped

into 50 mL of ethylene glycol solution with 4 mL of $Bi_5H_9N_4O_{22}$ solution under agitation. In order to ensure uniform doping, 50 mL of aqueous ammonium metavanadate (NH_4VO_3) solution was added slowly over 30 min and stirred for 4 h at 25°C. The suspension was then transferred to a Teflon-lined autoclave and treated hydrothermally at 120 °C for 36 h. It was cooled to room temperature, and Mn–$BiVO_4$ nanosheets were obtained, washed with DIW, and dried at 60 °C. Control of doping levels was achieved by precisely adjusting the Mn precursor concentration, while all other parameters (temperature, reaction time, solvent composition) were kept constant. Repeated syntheses confirmed reproducibility, with consistent XRD and FTIR patterns obtained across all batches.

2.4. Synthesis of Mn-$BiVO_4$/B-Ti_3C_2

The hybrid nanostructure Mn–$BiVO_4$/B–Ti_3C_2 was fabricated by a solution-phase self-assembly approach assisted by ultrasonic dispersion and magnetic stirring. In general, 15 mg of Mn–$BiVO_4$ and 15 mg of B–Ti_3C_2 were co-dispersed into a mixed solvent of 100 mL (H_2O/EtOH, v/v = 1:1) to enhance colloidal stability and ensure uniform hybridization. The suspension was sonicated (40 kHz, 200 W, 30 min) at 25 °C room temperature to achieve effective exfoliation and homogenization of the nanosheets. The blend was subsequently stirred magnetically for 1.5 h to optimize interfacial coupling of Mn–$BiVO_4$ and B–Ti_3C_2. The resulting hybrid was subsequently filtered under vacuum and vacuum-dried at 80 °C for 24 h in an attempt to eliminate the residual solvents and stabilize the nanocomposite. Control of the hybrid composition was achieved by maintaining a 1:1 weight ratio of Mn–$BiVO_4$ to B–Ti_3C_2 in all syntheses, while keeping solvent composition, sonication power, and reaction time constant. For comparison, other heterostructures including $BiVO_4$/B-Ti_3C_2, Mn-$BiVO_4$/Ti_3C_2, and Ti_3C_2/$BiVO_4$ were fabricated by replacing the respective precursors by following the same protocol.

3. Results and Discussion

3.1. Characterization of the samples

3.1.1. The effect of doping and coupling on chemical bonds

Fourier-transform infrared (FTIR) spectroscopy was employed to investigate the chemical bonding characteristics and functional group modifications resulting from doping and coupling in the synthesized nanostructures. As depicted in Fig. 1a, the FTIR spectrum of pristine Ti_3C_2 MXene exhibits characteristic peaks at 616.15 cm^{-1}, 955.38 cm^{-1}, and 1633.84 cm^{-1}, corresponding to the Ti–O stretching, C–F stretching, and C=O stretching vibrations, respectively. Additionally, a broad absorption band within the range of 3000–3500 cm^{-1} is attributed to the O–H stretching vibrations, indicative of surface-terminated hydroxyl groups, which enhance hydrophilicity and facilitate interaction with other nanomaterials. The FTIR spectrum of $BiVO_4$ (Fig. 1b) was previously reported in our work [31], and is reproduced here for comparison with the newly synthesized doped samples. Peaks at 550 cm^{-1}, 884 cm^{-1}, and 960 cm^{-1}, corresponding to V–O–V bridging

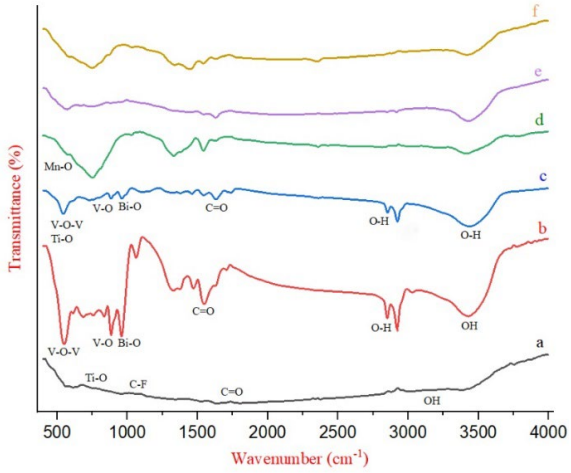

Fig. 1. FTIR spectra of **(a)** Ti_3C_2, **(b)** $BiVO_4$, **(c)** $BiVO_4$/Ti_3C_2, **(d)** Mn-$BiVO_4$/Ti_3C_2, **(e)** $BiVO_4$/B-Ti_3C_2, **(f)** Mn-$BiVO_4$/B-Ti_3C_2 of nanostructures.

vibrations, V–O stretching, and Bi–O stretching modes, respectively. A peak observed at 1548 cm^{-1} is attributed to the presence of carbonyl (C=O) groups, while additional absorption bands at 2804 cm^{-1}, 2917 cm^{-1}, and 3442 cm^{-1} correspond to O–H stretching, N–H bending, and hydroxyl (-OH) stretching vibrations, respectively. These functional groups play a crucial role in the interaction between $BiVO_4$ and Ti_3C_2 MXene during hybrid formation. Upon coupling of $BiVO_4$ with Ti_3C_2 and subsequent doping with Mn and B, significant spectral shifts and new vibrational modes emerge, confirming successful structural modification. As shown in Fig. 1c–1f, the presence of a distinct peak at 560.1 cm^{-1} corresponds to Mn–O stretching vibrations, verifying the incorporation of Mn within the $BiVO_4$ lattice in Mn-$BiVO_4$/Ti_3C_2 and Mn-$BiVO_4$/B-Ti_3C_2 nanostructures. The observed shifts in peak positions and intensities suggest changes in chemical bonding environments, likely due to electronic interactions and structural rearrangements induced by doping and coupling. These modifications are expected to influence the charge transfer dynamics and enhance the optical and electronic properties of the hybrid nanomaterials, making them promising candidates for advanced photocatalytic and optoelectronic applications.

3.1.2. The effect of doping and coupling on crystalline structure

X-ray diffraction (XRD) analysis was conducted to investigate the crystallographic phases and structural modifications induced by doping and coupling in the synthesized nanomaterials. As shown in Fig. 2a, the diffraction peaks at 2θ = 9.1°, 18.15°, 28.05°, 38.79°, and 60.45° correspond to the (002), (004), (006), (008), and (110) lattice planes of Ti_3C_2 MXene, respectively, confirming its characteristic layered structure. For pristine $BiVO_4$ (Fig. 2b), distinct diffraction peaks observed at 2θ = 17.28°, 17.97°, 29.03°, 32.62°, 35.52°, 40.23°, 43.54°, 46.72°, 48.11°, 55.85°, and 58.75° are indexed to the (110), (011), (121), (040), (200), (211), (015), (240), (042), (161), and (321) planes, respectively, which confirmed high purity of the monoclinic $BiVO_4$ phase (JCPDS No. 14-0688).

The addition of Ti_3C_2 to $BiVO_4$, as well as the addition of Mn and B dopants (including Fig. 2c–2f), gives rise to noticeable shifts in peaks as well as intensities. Specifically, the (110) peak of $BiVO_4$ shifts downward from 2θ = 17.28° to 18.77° after doping with Mn, corresponding to a decrease in interplanar spacing from 5.13 Å to 4.72 Å. This noticeable lattice contraction is consistent with the substitution of the larger-sized Bi^{3+} cations (1.17 Å) with the smaller-sized Mn^{2+} cations (0.80 Å). Similarly, the (002) peak of Ti_3C_2 moved downward from 2θ = 9.1° (d = 9.71 Å) to 7.02° (d = 12.58 Å) after being doped with B, indicating an increase of about 2.87 Å in interlayer separation, which may be attributed to the incorporation of boron species as well as their interactions with the surface-termination groups residing on Ti_3C_2.

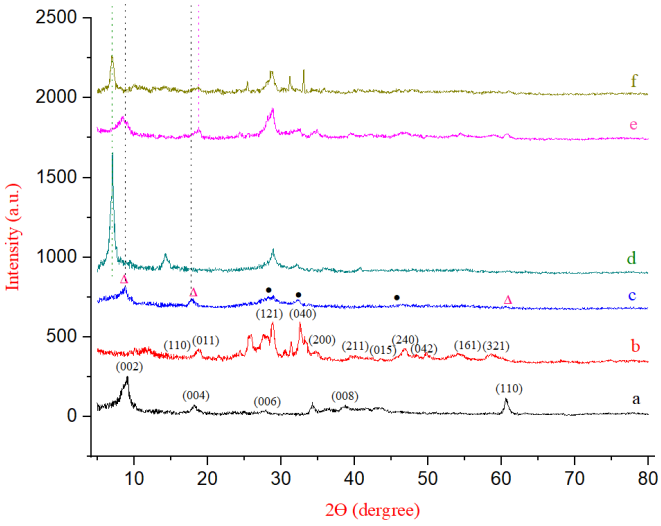

Fig. 2. XRD patterns of **(a)** Ti_3C_2, **(b)** $BiVO_4$, **(c)** $BiVO_4$/Ti_3C_2, **(d)** $BiVO_4$/ B-Ti_3C_2, **(e)** Mn-$BiVO_4$/ Ti_3C_2, **(f)** Mn-$BiVO_4$/B-Ti_3C_2 nanostructures

A comparative analysis of Fig. 2c ($BiVO_4/Ti_3C_2$) and Fig. 2f ($Mn–BiVO_4/B–Ti_3C_2$) supports the successful construction of the hybrid structure, as evidenced by the appearance of the Ti_3C_2 and $BiVO_4$ peaks, together with corresponding shifts. The results present that the doping of Mn and B introduces noticeable lattice deformities, as expected to influence considerably charge transport as well as photocatalytic activity.

3.1.3. The effect of doping and coupling on size and morphology

Field-emission scanning electron microscopy (FESEM) was also used to study the dimensional changes and morphological features caused by doping and coupling of the nanostructures that are being synthesized. Fig. 3 shows FESEM images of the respective composites of the $BiVO_4/Ti_3C_2$ and $Mn\text{-}BiVO_4/B\text{-}Ti_3C_2$ composites. From Fig. 3(a) and 3(b), it is portrayed that the $BiVO_4/Ti_3C_2$ composite has a heterogeneous sheet-like structure, wherein ultrathin nano-sheets of $BiVO_4$ are dispersed on the broader Ti_3C_2 MXene sheets. The nano-sheets of $BiVO_4$ are of an average thickness of around 10 ± 2 nm and of varying lateral dimensions of 50 to 150 nm, supporting the nature of nanosheet growth. Irregular distribution of $BiVO_4$ reveals partial coverage, thus likely affecting interfacial charge transfer nature.

After doping with Mn (Fig. 3(c, d)), there is a sudden increase in the lateral dimension of the $BiVO_4$ nanosheets and a higher stacking tendency in the $Mn\text{-}BiVO_4/B\text{-}Ti_3C_2$ hybrid material. Doping with Mn appears to promote lateral sheet growth and partial agglutination of the nanosheets, due to interlayer interaction and surface charge distribution changes. As a consequence of induced changes in morphology brought about through doping with Mn, the electronic structure, charge carrier transport, and catalytic ability of the hybrid material are likely to be modified.

3.1.4. The effect of doping on elemental distribution

Energy-dispersive X-ray spectroscopy (EDX) analysis and elemental mapping were performed to assess the elemental composition and spatial distribution of constituent elements in the synthesized nanostructures. Fig. 4 presents the EDX spectra and elemental mapping images of $BiVO_4/Ti_3C_2$ and $Mn\text{-}BiVO_4/B\text{-}Ti_3C_2$ composites. The elemental mapping confirms a homogeneous and uniform distribution of Bi, V, Ti, Mn, and O in the $Mn\text{-}BiVO_4/B\text{-}Ti_3C_2$ composite, suggesting

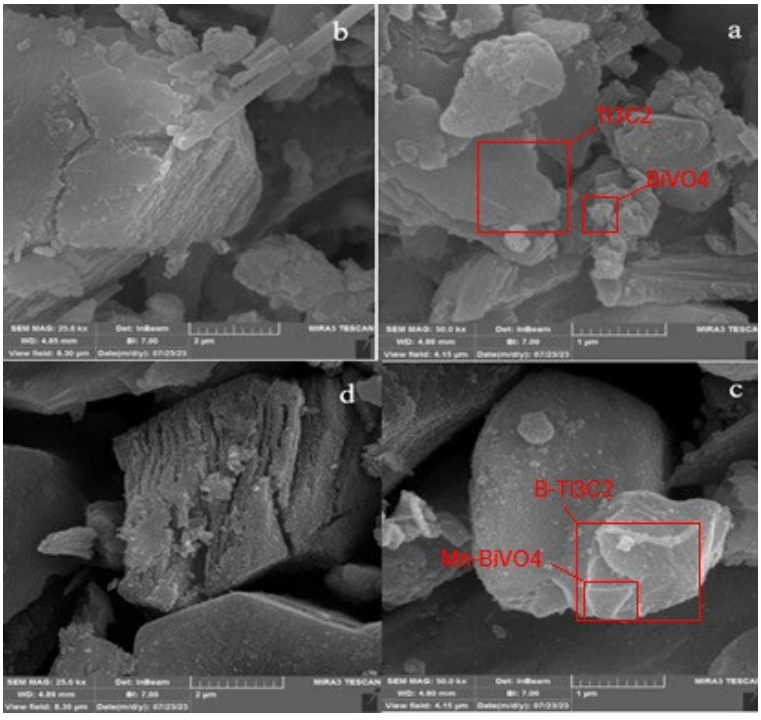

Fig. 3. FESEM images of (a,b)$BiVO_4/ Ti_3C_2$, (c,d) $Mn\text{-}BiVO_4/ B\text{-}Ti_3C_2$ photocatalysts

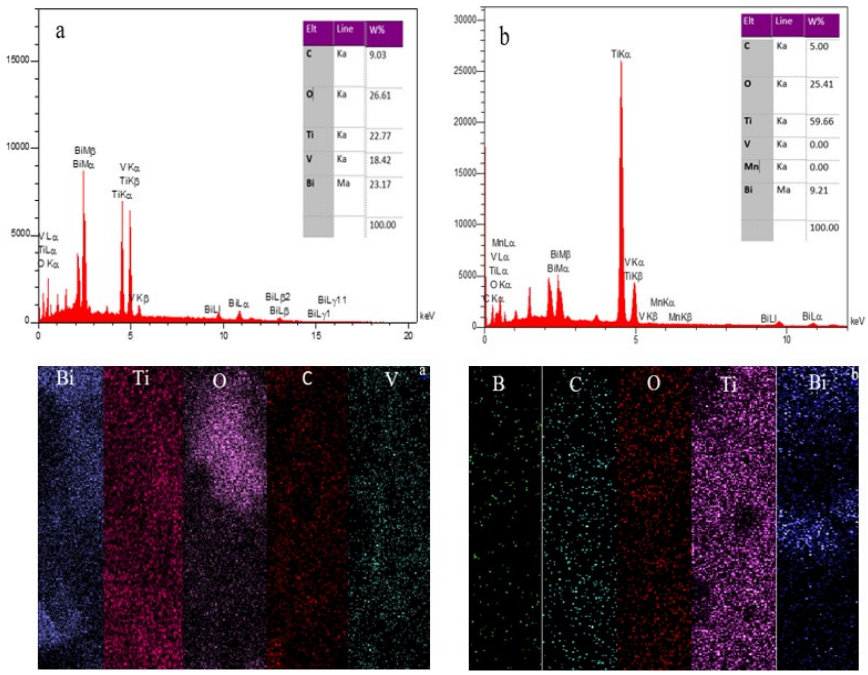

Fig. 4. EDX spectra and elemental distribution map of **(a)** $BiVO_4/Ti_3C_2$, **(b)** Mn-$BiVO_4$/B-Ti_3C_2 photocatalysts

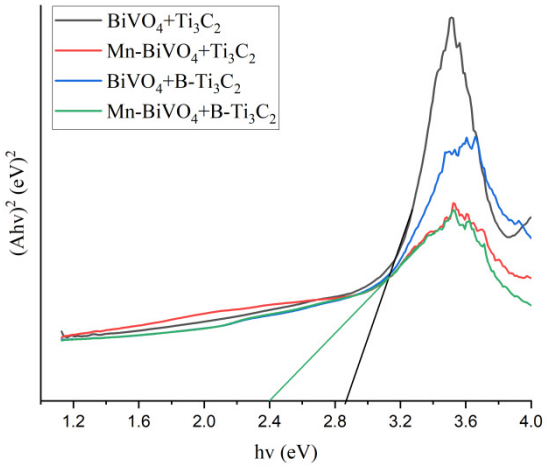

Fig. 5. Tauc plot of nanostructures

successful doping and coupling. This technique is not able to identify the boron element.

3.1.5. The effect of doping on band gap and optical properties

Ultraviolet-visible (UV-Vis) spectroscopy was utilized to evaluate the optical absorption characteristics. To determine the optical band gap (Eg), Tauc's equation was employed:

$$(Ahυ)^2=B(hυ-E_g)$$

where A represents absorbance, hν denotes photon energy, B is a proportionality constant, and Eg is the band gap energy [32]. By extrapolating the linear portion of the Tauc plot (Fig. 5b), the direct optical band gap of Mn-$BiVO_4$/B-Ti_3C_2 was estimated to be 2.4 eV, which is lower than that of the undoped samples. This reduction in band gap energy can be attributed to the introduction of

Mn^{2+} ions, which create localized electronic states within the band structure, facilitating enhanced photon absorption and improved charge carrier separation. These results confirm that Mn and B doping effectively tunes the electronic and optical properties of the $BiVO_4/Ti_3C_2$ system, making it a promising candidate for advanced photocatalytic and optoelectronic applications.

4. Conclusion

This study demonstrates that Mn and B doping, combined with 2D/2D heterostructure formation, effectively modulates the structural, optical, and electronic properties of Ti_3C_2 MXene and $BiVO_4$ nanosheets. The proposed Mn-$BiVO_4$/B-Ti_3C_2 hybrid displays enhanced light absorption, a narrowed band gap, and improved charge separation, indicating its great potential for photocatalytic hydrogen evolution. Future work efforts are intended to focus on the optimization of doping levels, elucidating charge transfer mechanisms, and evaluating long-term stability to advance practical applications in solar-driven water splitting and other photo-driven redox processes.

Conflicts of Interest

The authors declare that they have no known competing financial interests or personal relationships that could have appeared to influence the work reported in this paper.

References

[1] V. Mohammadi, J. Rosen, Y. Gogotsi, The world of two-dimensional carbides and nitrides (MXenes), Science, 372 (2021) 1581. https://doi.org/10.1126/science.abf158

[2] Z. Chen, X. Duan, W. Wei, S. Wang, B.-J. Ni, Recent advances in transition metal-based electrocatalysts for alkaline hydrogen evolution, J. Mater. Chem. A, 7(25) (2019) 14971–15005. https://doi.org/10.1039/C9TA03220G

[3] Y. Vasseghian, E.N. Dragoi, F. Almomani, A comprehensive review on MXenes as new nanomaterials for degradation of hazardous pollutants: Deployment as heterogeneous sonocatalysis, Chemosphere, 287 (2022) 132387. https://doi.org/10.1016/j.chemosphere.2021.132387

[4] N. Devi, R. Kumar, R. Kumar Singh, S.A. Moshkalev, Recent development of MXenes and their composites in electrochemical energy storage: Current status, challenges and future prospects, J. Power Sources, 636 (2025) 236538. https://doi.org/10.1016/j.jpowsour.2025.236538

[5] F. Fathirad, E. Sadeghi, $NiFe_2O_4/Ti_3C_2$ nanocomposite as an efficient catalyst for methanol electro-oxidation reaction: Investigating annealing temperature and synergetic effect, Fuel, 358 (2024) 130130. https://doi.org/10.1016/j.fuel.2023.130130

[6] Z. Chen, J. Cao, X. Wu, D. Cai, M. Luo, S. Xing, X. Wen, Y. Chen, Y. Jin, D. Chen, Y. Cao, B/N Co-doping sequence: An efficient electronic modulation of the Pd/MXene interface with enhanced electrocatalytic properties for ethanol electrooxidation, ACS Appl. Mater. Interfaces, 14(10) (2022) 12223–12233. https://doi.org/10.1021/acsami.1c23718

[7] J. Chen, X. Yuan, F. Lyu, Q. Zhong, H. Hu, Q. Pan, Q. Zhang, Integrating MXene nanosheets with cobalt-tipped carbon nanotubes for an efficient oxygen reduction reaction, J. Mater. Chem. A, 7(3) (2019) 1281–1286. https://doi.org/10.1039/C8TA10574J

[8] I.A. Alsafari, S. Munir, S. Zulfiqar, M.S. Saif, M.F. Warsi, M. Shahid, Synthesis, characterization, photocatalytic and antibacterial properties of copper ferrite/MXene ($CuFe_2O_4/Ti_3C_2$) nanohybrids, Ceram. Int., 47(20) (2021) 28874–28883. https://doi.org/10.1016/j.ceramint.2021.07.048

[9] Z. Wang, K. Yu, Y. Feng, R. Qi, J. Ren, Z. Zhu, Stabilizing Ti_3C_2Tx-MXenes with TiOF2 nanospheres intercalation to improve hydrogen evolution reaction and humidity-sensing performance, Appl. Surf. Sci., 496 (2019) 143729. https://doi.org/10.1016/j.apsusc.2019.143729

[10] A. Kudo, K. Omori, H. Kato, A novel aqueous process for preparation of crystal form-controlled and highly crystalline $BiVO_4$ powder from layered vanadates at room temperature and its photocatalytic and photophysical properties, J. Am. Chem. Soc., 121(49) (1999) 11459–11467. https://doi.org/10.1021/ja992541y

[11] S. Tokunaga, H. Kato, A. Kudo, Selective preparation of monoclinic and tetragonal $BiVO_4$ with scheelite structure and their photocatalytic properties, Chem. Mater., 13(12) (2001) 4624–4628. https://doi.org/10.1021/cm0103390

[12] S. Kohtani, A.S. Makino, A. Kudo, K. Tokumura, Y. Ishigaki, Photocatalytic degradation of 4-n-nonylphenol under irradiation from solar simulator: Comparison between $BiVO_4$ and TiO_2 photocatalysts, Chem. Lett., 31 (2002) 660–661. https://doi.org/10.1246/cl.2002.660

[13] X. Du, T. Zhao, Z. Xiu, Z. Xing, Li Z., Pan K., Yang S., Zhou W., $BiVO_4$@$ZnIn_2S_4/Ti_3C1111000$ MXene quantum dots assembly all-solid-state direct Z-Scheme photocatalysts for efficient visible-light-driven overall water splitting, Appl. Mater. Today, 20 (2020) 100719. https://doi.org/10.1016/j.apmt.2020.100719

[14] P. Dagar, S. Kumar, A.K. Ganguli, Effect of Mn^{2+} incorporation on the photoelectrochemical properties of BiVO4, J. Chem., 46(6) (2022) 2875–2886. https://doi.org/10.1039/D1NJ05292F

[15] J. Joy, J. Mathew, S.C. George, Nanomaterials for photoelectrochemical water splitting–review, Int. J. Hydrogen Energy, 43(10) (2018) 4804-4817. https://doi.org/10.1016/j.ijhydene.2018.01.099

[16] Y. Peng, Y. Shi, S. Yan, G. Li, Photocarrier behavior and photocatalytic H_2O_2 synthesis performance of amorphous/crystalline $SrTiO_3/BiVO_4$ layered heterostructures, Renew. Energy, 237 (2024) 121686. https://doi.org/10.1016/j.renene.2024.121686

[17] B. Alshahrani, S. Saad Fares, R. Saleh Alqurashi, M. Salman, A.H. Korna, Effect of gamma irradiation on the structural, optical, and electronic properties of PVC/$BiVO_4$/ZnO nanocomposite films, Phys. Open, 23 (2025) 100252. DOI: 10.1016/j.physo.2025.100252

[18] H. Wang, Y. Bai, R. Wang, Y. Fu, Q. Mei, B. Bai, Q. Wang,

Boosting photoelectrochemical water splitting: Enhanced hole transport in BiVO4 photoanodes via interfacial coupling, Catal. Sci. Technol., 15 (2024) 405–415. https://doi.org/10.1039/D4CY01284D

[19] Z. Fu, Y. Zhu, D. Qin, Y. Yang, S. Han, Z. Dong, Functional coupling hole transport and extraction units over $BiVO_4$ for efficient solar-to-hydrogen conversion, Energy Convers. Manag., 322 (2024) 119153. https://doi.org/10.1016/j.enconman.2024.119153

[20] C. Feng, X. Jia, X. Shao, X. Cheng, F. Zhan, Y. Zhang, Z. Bian, K. Zhao, F. Yu, Z. Wang, Doping engineering achieves $BiVO_4$ and hematite band matching accelerating photoelectrochemical water splitting, Fuel, 387 (2025) 134457. https://doi.org/10.1016/j.fuel.2025.134457

[21] D. Afzali, B. Bahadori, F. Fathirad, Ultrasound-assisted emulsification/microextraction based on solidification of trace amounts of thallium prior to graphite furnace atomic absorption spectrometry determination, Toxicol. Environ. Chem., 95(7) (2013) 1080–1089. https://doi.org/10.1080/02772248.2013.856912

[22] C. Zhou, Y. Hu, Z. Zhang, T. Shen, J. Song, R. Guan, Y. Guan, B-doped $BiVO_4$/Bi nanocomposites activated persulfate for efficient photocatalytic degradation of levofloxacin, Sep. Purif. Technol., 359 (2025) 130557. https://doi.org/10.1016/j.seppur.2024.130557

[23] X. Fan, H. Liang, Y. Song, Z. Xing, J. Bai, Development of a novel beads-like In/Fe co-doped $BiVO_4$ composite for enhanced photocatalytic degradation of tetracycline in water, Colloids Surf. A: Physicochem. Eng. Aspects, 687 (2024) 133477. https://doi.org/10.1016/j.colsurfa.2024.133477

[24] T. Iqbal, M. T. Qureshi, R. Shahzad, S. Afsheen, S. Kausar, G. Yunus, M.S. Mansha, L. Aamir, R. M. Munir, H.A. El-Serehy, M.Y. Khan, B.M. Al-Maswari, Synergistic impacts of novel tantalum doping in BiVO4 for effective photocatalytic applications, antimicrobial activity, and antioxidant aspect, Inorg. Chem. Commun., 170 (2024) 113365. https://doi.org/10.1016/j.inoche.2024.113365

[25] W. Wang, M. Fan, Z. Zhang, L. Wu, Y. Liu, Y. Cao, W. Peng, In-situ nanofication of Cu-doped $BiVO_4$ on montmorillonite nanosheets with enhanced photocatalytic efficiency for phenolic degradation, Sep. Purif. Technol., 361 (2025) 131341. https://doi.org/10.1016/j.seppur.2024.131341

[26] J. Zheng, Z. Zhao, J. Liang, B. Liang, H. Huang, G. Huang, M. Junaid, J. Wang, K. Huang, Simultaneous photocatalytic removal of tetracycline and hexavalent chromium by $BiVO_4$/0.6CdS photocatalyst: Insights into the performance, evaluation, calculation and mechanism, J. Colloid Interface Sci., 667 (2024) 650–662. https://doi.org/10.1016/j.jcis.2024.04.127

[27] V. Balakumar, C. Chuaicham, K. Sasaki, K. Sekar, Fabrication of $BiVO_4$/reduced graphene oxide photocatalyst for hexavalent chromium reduction under visible region, Mater. Today, 50 (2022) 400–405. https://doi.org/10.1016/j.matpr.2021.11.381

[28] D. Afzali, F. Fathirad, S. Ghaseminezhad, Z. Afzali, Determination of trace amounts of zirconium in real samples after microwave digestion and ternary complex dispersive liquid–liquid microextraction, Environmental monitoring and assessment, 186 (6) (2014) 3523-3529. https://doi.org/10.1007/s10661-014-3635-7

[29] Y. Liu, R. Zhao, D. Yu, Efficient detection and degradation of hexavalent chromium wastewater in tourist attractions using dual-fluorescent UiO-66-NH_2 stabilized polysulfone Pickering emulsions, Colloids Surf. A: Physicochem. Eng. Aspects, 706 (2025) 135812. https://doi.org/10.1016/j.colsurfa.2024.135812

[30] A. Raja, P. Rajasekaran, B. Vishnu, K. Selvakumar, J.Y. Do, M. Swaminathan, M. Kang, Fabrication of effective visible-light-driven ternary Z-scheme ZnO-Ag-$BiVO_4$ heterostructured photocatalyst for hexavalent chromium reduction, Sep. Purif. Technol., 252 (2020) 117446. https://doi.org/10.1016/j.seppur.2020.117446

[31] F. Soltaninezhad, F. Fathirad, Synthesis and characterization of g-C_3N_4/$BiVO_4$ nanosheets: Exploring the effect of doping and heterostructure coupling on photoelectrochemical performance, Diam. Relat. Mater., 159 (2025) 112760. https://doi.org/10.1016/j.diamond.2025.112760

[32] F. Qureshi, M. Tahir, Photoelectrochemical water splitting with engineering aspects for hydrogen production: Recent advances, strategies and challenges, Int. J. Hydrogen Energy, 69 (2024) 760–776. https://doi.org/10.1016/j.ijhydene.2024.05.039